

# Development of Graphene Oxide/Polyaniline Inks for High Performance Flexible Microsupercapacitors via Extrusion Printing

Yuqing Liu, Binbin Zhang, Qun Xu, Yuyang Hou, Shayan Seyedin, Si Qin, Gordon G. Wallace,\* Stephen Beirne, Joselito M. Razal, and Jun Chen\*

Extrusion printing of interdigitated electrodes for flexible microsupercapacitors (fMSCs) offers an attractive route to the fabrication of flexible devices where cost, scalability, and processability of ink formulations are critical. In this work, highly concentrated, viscous, and water-dispersible inks are developed based on graphene oxide (GO)/polyaniline (PANI) composite for extrusion printing. The optimized GO/PANI-based all-solid-state symmetric fMSCs obtained by extrusion printing interdigitated microelectrodes can deliver outstanding areal capacitance of  $153.6 \text{ mF cm}^{-2}$  and volumetric capacitance of  $19.2 \text{ F cm}^{-3}$  at  $5 \text{ mV s}^{-1}$ . It is shown that by fabricating asymmetric fMSCs using the GO/PANI as positive electrode and a graphene-based negative electrode, the voltage window can be widened from 0.8 to 1.2 V and improvements can be achieved in energy density (from  $3.36$  to  $4.83 \text{ mWh cm}^{-3}$ ), power density (from  $9.82$  to  $25.3 \text{ W cm}^{-3}$ ), and cycling stability (from 75% to 100% capacitance retention over 5000 cycles) compared with the symmetric counterpart. The simple ink preparation and facile device fabrication protocols reported here make the scalable fabrication of extrusion printed fMSCs a promising technology.

## 1. Introduction


Flexible microsupercapacitors (fMSCs), which possess various merits like simple structure, ease for large scale production, and superior electrochemical properties (i.e., high energy and

power density, fast charge–discharge and extremely long cycle life) are being widely studied as an energy storage unit for portable and/or wearable microelectronics.<sup>[1–4]</sup> Design configurations have previously relied on a stacked arrangement (i.e., two planar film electrodes facing each other separated by electrolyte). More recently an interdigitated planar design arrangement (i.e., electrode fingers interdigitally arranged on insulating substrates) is gaining attention in fMSCs. This alternative design enables effective space utilization of electrode materials and improved electrolyte penetration and a short ion transfer pathway, which result in high energy and power densities from a limited space.<sup>[5–9]</sup> However, the use of conventional microelectrode patterning poses limitations on the scalable fabrication of interdigitated fMSCs. For example, lithography can make elaborate fMSC patterns based on a wide range of active materials

including carbon materials (e.g., graphene<sup>[10–13]</sup> and carbon nanotubes<sup>[14,15]</sup>), conducting polymers (e.g., polypyrrole<sup>[7]</sup> and polyaniline (PANI)<sup>[16]</sup>), metal oxides (e.g., manganese oxide<sup>[17]</sup>) as well as carefully designed nanostructured composite materials (e.g., graphene/PANI<sup>[18]</sup> and graphene oxide (GO)/MnO<sub>2</sub>/silver nanowires<sup>[19]</sup>). Excellent performances have been achieved for these fMSCs. Nevertheless, their sophisticated processing and high cost make the production of lithography-based fMSCs in mass quantities rather challenging. Novel and scalable patterning techniques including laser-writing and laser-etching have been recently applied to large-size film electrode sheets to generate symmetric interdigitated microelectrode patterns.<sup>[20–27]</sup> These techniques are simple, low-cost and allow for facile adjustment of the electrode and device design. However, the fabrication of asymmetric fMSCs for the improvement of the operating voltage window on a single device requires several tedious steps (such as electrodeposition of metal oxides<sup>[28,29]</sup> and conducting polymers<sup>[28]</sup>), which can increase the cost on industrial scale fabrication. In addition, the significant volumes of waste materials (i.e., etched and unused materials) cannot be avoided in these methods.

Direct printing of active materials is an attractive alternative method for the fabrication of fMSCs.<sup>[30–32]</sup> It provides a simple,

Y. Liu, Dr. B. Zhang, Y. Hou, Prof. G. G. Wallace,  
Dr. S. Beirne, Prof. J. Chen  
Intelligent Polymer Research Institute and ARC Centre of Excellence  
for Electromaterials Science  
University of Wollongong  
Wollongong, NSW 2500, Australia  
E-mail: gwallace@uow.edu.au; junc@uow.edu.au  
Prof. Q. Xu  
College of Materials Science and Engineering  
Zhengzhou University  
Zhengzhou 450052, China  
Dr. S. Seyedin, Dr. S. Qin, Prof. J. M. Razal  
Institute for Frontier Materials  
Deakin University  
Geelong, VIC 3216, Australia

 The ORCID identification number(s) for the author(s) of this article can be found under <https://doi.org/10.1002/adfm.201706592>.

DOI: 10.1002/adfm.201706592

high speed, and scalable approach and allows fabrication of microelectrodes with a high degree of flexibility in the patterns and geometries. The ability to produce asymmetric fMSCs in a simple way (i.e., by changing printing inks) and to control electrode thickness (i.e., through the addition of further material layers via additive printing) may also provide some advantages in terms of design flexibility compared to laser-based etching techniques. Among various printing techniques, inkjet printing has been widely used to prepare fMSCs. Li et al.<sup>[33]</sup> have shown scalability in fabricating fMSCs by inkjet printing large-scale fMSC arrays (12 series  $\times$  12 parallel) on flexible Kapton (a commercialized polyimide film). Asymmetric fMSCs based on lamellar  $\text{K}_2\text{Co}_3(\text{P}_2\text{O}_7)_2 \cdot 2\text{H}_2\text{O}$  nanocrystal whiskers and graphene nanosheets were also prepared by printing both the positive and negative electrode materials.<sup>[34]</sup> However, the processing efficiency is low due to the low solid concentration of inks to ensure compatibility with the inkjet process. Extrusion-based 3D printing, which extrudes viscous inks through a deposition nozzle, is expected to provide higher efficiency.<sup>[32,35]</sup> However, to date there are only a few reports on symmetric fMSCs based on carbon materials (i.e., graphene<sup>[35]</sup> and carbon nanotube<sup>[32]</sup>) and no report on asymmetric fMSCs or fMSCs based on pseudocapacitive materials using extrusion printing techniques. The main obstacle for realizing this technology is the development of appropriate active material ink formulations that meet the extrusion printing processing requirements.

Extrusion printing requires inks with high stability, high viscosity, and homogeneous dispersion of active materials. In recent years, stable suspensions containing capacitive materials (e.g., graphene,<sup>[36–39]</sup> carbon nanotube,<sup>[32]</sup> polyaniline<sup>[40–43]</sup>) have been prepared. Strategies to disperse these insoluble materials involve either careful selection of organic solvents or using polymer stabilizers or surfactants. However, these approaches present the following challenges. (i) The use of toxic or flammable solvents (e.g., dimethylformide, *N*-methyl-2-pyrrolidone, isopropanol, acetone) needs exhaust and carriage systems and poses safety concerns for mass production of fMSCs. (ii) The electrical conductivity and electroactivity of the materials are affected by the insulating stabilizers or surfactants and post-treatment (e.g., high temperature annealing) required to eliminate these additives is not compatible with most of the flexible substrates (i.e., plastics, papers and textiles). (iii) The concentration of active materials in these inks is usually very low (mostly less than  $10 \text{ mg mL}^{-1}$  and sometimes less than  $1 \text{ mg mL}^{-1}$ ) which results in low viscosity and thus makes it difficult to achieve fine and constant lines during the extrusion. (iv) Present inks mainly contain a single active nanocarbon (e.g., graphene, carbon nanotubes, etc.) or pseudocapacitive material (e.g., PANi,  $\text{K}_2\text{Co}_3(\text{P}_2\text{O}_7)_2 \cdot 2\text{H}_2\text{O}$ ,<sup>[34]</sup>  $\text{Ni}(\text{OH})_2$ ,<sup>[44]</sup> etc.). Inks containing the hybrid of nanocarbon and pseudocapacitive material were not developed up to date. Such materials were reported to exhibit superior performance (i.e., higher capacitance and rate capability) in lithography-based and laser-etched fMSCs,<sup>[18,28]</sup> due to robust nanostructures (e.g., nanostructured pseudocapacitive materials on carbon templates) and synergistic effects (i.e., high conductivity and stability from carbon materials, excellent capacitance from pseudocapacitive materials).

We build on our previous work on aqueous composite formulations of reduced graphene oxide (RGO) and

poly(3,4-ethylenedioxythiophene): poly(styrenesulfonate) (PEDOT: PSS) (denoted as RGO-PE) in making viscous inks for extrusion printing. In this work, we make new composite formulations by growing vertically aligned pseudo-capacitive PANi nanorods on both sides of the GO surface. Here, the conductive PEDOT: PSS also functions as the stabilizer for the GO/PANi composite sheets. By tuning the synthesis conditions and formulation composition, we achieve aqueous-based GO/PANi-PEDOT: PSS (GO/PA-PE) inks with suitable rheological properties for extrusion printing. Upon printing, the microelectrodes can be directly used for the fabrication of fMSCs without any postprocessing (e.g., no heat treatment required to remove additives). By repeatedly printing up to 20 layers of GO/PA-PE, we achieve a symmetric fMSC device that can deliver outstanding device areal capacitance of  $153.6 \text{ mF cm}^{-2}$  and volumetric capacitance of  $19.2 \text{ F cm}^{-3}$  at  $5 \text{ mV s}^{-1}$ . We show that it is also possible to fabricate an asymmetric fMSC comprising GO/PA-PE as positive electrode and RGO-PE as negative electrode which demonstrates improvements in voltage window (from 0.8 to 1.2 V), energy density (from 3.36 to  $4.83 \text{ mWh cm}^{-3}$ ), power density (from 9.82 to  $25.3 \text{ W cm}^{-3}$ ), and cycling stability (from 75% to 100% capacitance retention over 5000 cycles) compared with the symmetric GO/PA-PE fMSCs.

## 2. Results and Discussions

### 2.1. Printable Inks and Extrusion Printing Process

Figure 1a shows the facile preparation process of aqueous-based GO/PA-PE composite inks. We first vertically attached PANi nanorods on the GO sheets using an interfacial polymerization approach and obtained a GO/PANi composite with well-defined nanostructure. We then utilized electroactive PEDOT: PSS as a dispersing agent to achieve highly dispersed water-based GO/PA-PE inks that could meet the stability requirement of extrusion printing. We observed that the GO/PANi composite was not water dispersible (Figure 1b), although GO sheets have very high dispersibility in water.<sup>[35]</sup> Scanning electron microscopy (SEM) observations (Figure 1b) revealed that the GO sheets were fully covered by water insoluble PANi nanorods during the polymerization process, which could prevent the access of various hydrophilic functional groups of GO (e.g., hydroxyl and carboxyl). We utilized the high electrostatic interactions of the negatively charged  $\text{HSO}_3$  groups of PSS with the positively charged anilinium ions of PANi reported previously,<sup>[40,45]</sup> and attached PEDOT: PSS onto PANi nanorods. SEM studies (Figure 1c) showed that the GO surface morphology changed from vertically aligned sharp protrusions to a much smoother surface, which can be explained by the PEDOT: PSS wrapping of PANi nanorods. The GO/PA-PE could be dispersed very well in water (Figure 1c, photo), due to the presence of water-dispersible PEDOT: PSS covering the nanostructured GO/PANi composite. We investigated the effect of GO/PANi weight ratio on dispersibility of GO/PA-PE composites. Precipitations and sediments in the GO/PA-PE dispersion were observed when the GO/PANi loading in the composite was above  $\approx 50 \text{ wt\%}$  (Figure S1, Supporting Information). The GO/PA-PE dispersions with less than  $\approx 50 \text{ wt\%}$  GO/PANi remained

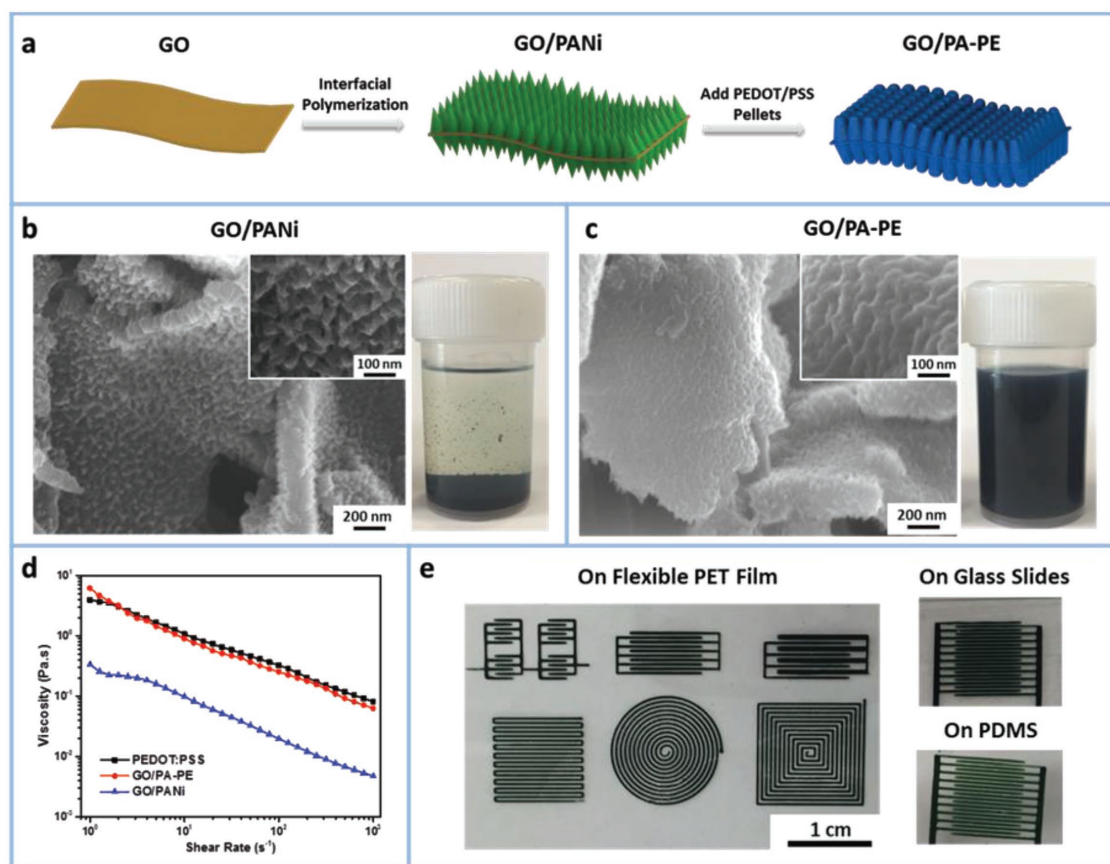


**Figure 1.** a) Schematic illustration of the preparation of dispersible GO/PA-PE inks. Scanning electron microscopy (SEM) images and digital photographs of b) GO/PANI and c) GO/PA-PE composites and dispersions. d) The changes in various ink viscosities as a function of shear rate. e) Digital photographs of extrusion printed GO/PA-PE patterns on various substrates.

homogeneous and sediment-free for more than 1 d (also confirmed by optical microscopy and ultraviolet–visible (UV–vis) spectra in Figures S2 and S3, Supporting Information), which was sufficient to allow their printing and thus these dispersions were investigated further.

We also investigated the rheological properties of GO/PA-PE to identify compositions and formulations that have suitable properties for extrusion printing, i.e., high viscosity and shear thinning behavior. Having an ink that shows high viscosity at a low shear rate is necessary for the extrusion printing process because the high viscosity prevents the ink from immediately spreading on the substrate extrusion and thus can form constant lines along the movement direction of the nozzle.<sup>[30,32]</sup> A good flowability at printing shear rate is also required to make sure the ink can easily flow through the printing nozzles under the applied pressure, thus a shear thinning behavior of the ink is favorable.<sup>[30]</sup> We achieved pure PEDOT: PSS dispersions with a concentration up to 25 mg mL<sup>−1</sup> that showed a viscosity of ≈3.9 Pa s at a low shear rate of 1 s<sup>−1</sup> (Figure S4, Supporting Information) high enough for extrusion printing (0.2–10<sup>4</sup> Pa s at 1 s<sup>−1</sup>)<sup>[32,46,47]</sup> to form fine lines on printing substrates when extruded from moving nozzles. Hence, we maintained the concentration of PEDOT: PSS at 25 mg mL<sup>−1</sup> in all GO/PA-PE composite dispersions to achieve reliable printing. Rheological measurements showed that the composite ink with

the GO/PANI loading of ≈50 wt% had similar shear thinning behavior and a slightly higher viscosity (≈6.1 Pa s at 1 s<sup>−1</sup>) than the pure PEDOT: PSS ink, which was also within the extrusion printing range. The printing shear rate ( $\dot{\gamma}$ ) of the GO/PA-PE ink was calculated as 833 s<sup>−1</sup> from the Equation (1),<sup>[48]</sup> in which the ink flow rate ( $Q$ ) was kept at 5  $\mu$ L min<sup>−1</sup> and nozzles with inner radius ( $R$ ) of 50  $\mu$ m was used in all printing process. The low viscosity (0.07 Pa s) of the GO/PA-PE ink at this shear rate indicates the good flowability of the ink.

$$\dot{\gamma} = \frac{4Q}{\pi R^3} \quad (1)$$

Figure 1e displays the versatility of extrusion printing in making various patterns using the GO/PA-PE ink (50 wt% GO/PANI loading), on a variety of substrates including polyethylene terephthalate (PET), polydimethylsiloxane (PDMS), and glass. Well-defined patterns such as interdigitated electrodes (with different finger widths and distances), antennas (with curves and straight lines), and electronic circuits could be printed by simply changing the computer-aided design. The minimum line width of ≈200  $\mu$ m was printed using a microneedle with an inner diameter of 100  $\mu$ m (Figure 2b and Figure S5, Supporting Information), which can be further minimized using needles with smaller nozzle diameters. The contact angle between ink



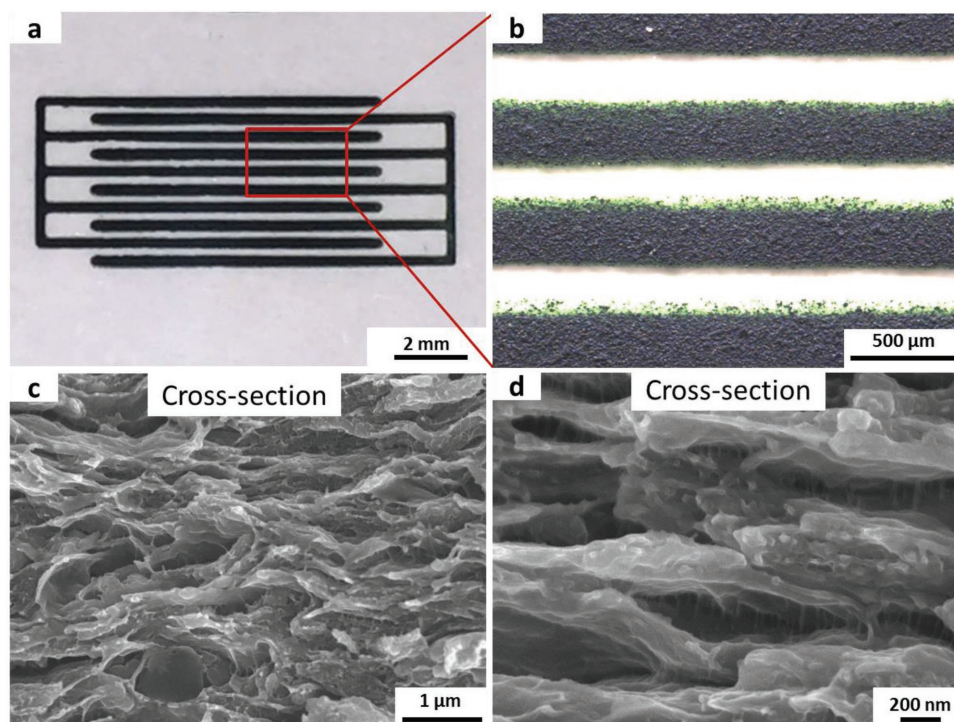


**Figure 2.** a,b) Optical microscopy and c,d) cross-sectional SEM images of extrusion printed interdigitated electrodes.

and substrate needs to be tuned prior to printing. For example, when printing on substrates with poor wettability (contact angle  $>90^\circ$ ) discontinuous dots form on the substrate, instead of continuous lines; whereas on substrates with a low contact angle, the extruded ink will spread before drying, resulting in poor print resolution. Therefore, PET and PDMS substrates were treated with oxygen plasma to make them wettable (contact angles of  $48.8^\circ$  and  $46.6^\circ$ , respectively). Glass slides showed a contact angle of  $69.1^\circ$  and were thus used without treatment (Figure S6, Supporting Information). The extrusion printed GO/PA-PE lines from an ink with 50 wt% GO/PA loading showed an electrical conductivity of  $\approx 64 \text{ S cm}^{-1}$  (line width  $\approx 800 \mu\text{m}$  and thickness  $\approx 10 \mu\text{m}$ ), which is comparable with previous works on carbon<sup>[20,49]</sup> and conducting polymer<sup>[18,50]</sup> electrodes for supercapacitors. This result indicated that the GO/PA-PE printed lines can be used directly as electrodes for fMSCs without post-treatment.

We studied the cross-section morphology of five stacked layers of extrusion printed GO/PA-PE lines (Figure 2a) using SEM and observed a very well-defined layer-by-layer structure without any noticeable space between the printed layers (Figure 2c). This observation suggests a very good adhesion between the adjacent printing layers. While all layers were tightly packed (Figure S7, Supporting Information) to form seamless printed lines, some porous structures could be observed between the composite sheets (Figure 2d). This porous structure is highly desirable in fMSC applications as it is perceived to allow electrolyte penetration and to facilitate ion diffusion.

We monitored the structural evolutions at different stages of GO/PA-PE composite preparation using X-ray diffraction

(XRD), Raman spectroscopy, and Fourier-transform infrared spectroscopy (FTIR). XRD results showed a downshift in (002) diffraction of the GO from  $2\theta$  of  $\approx 9.1^\circ$  in the pure sample to  $\approx 7.0^\circ$  in the GO/PANi composite, which further decreased to  $\approx 6.7^\circ$  on the GO/PA-PE composite (Figure 3a). Concurrently, the interlayer  $d$ -spacing between the GO sheets, calculated from the Bragg's law<sup>[51]</sup> (Equation (S1), Supporting Information), increased from  $\approx 0.92 \text{ nm}$  (for the pristine GO) to  $\approx 1.31$  and  $\approx 1.37 \text{ nm}$  for the GO/PANi and GO/PA-PE, respectively. This gradual increase in the GO interlayer spacing confirmed our SEM observations (Figure 1b,c) that PANi nanorod and PEDOT: PSS wrapped around the GO sheets, which helped the GO sheets remain highly exfoliated and prevented their restacking. In addition, PANi diffractions at  $2\theta$  of  $\approx 18^\circ$  and  $\approx 26^\circ$ , which were present in the GO/PANi composite, became very weak in the GO/PA-PE composite indicating the coverage of PANi nanorods with PEDOT: PSS as observed in SEM studies (Figure 1b,c).

The Raman spectra of GO/PANi and GO/PA-PE composites showed the presence of all signature vibrations of PANi emeraldine salt (Figure 3b). These include the main vibrations in quinoid structure (i.e., in plane C–H bending at  $1169 \text{ cm}^{-1}$ , stretching of C–C, C=N, C–N, and C–C at  $1410$ ,  $1474$ , and  $1597 \text{ cm}^{-1}$ , respectively) and benzenoid rings (i.e., amine deformation at  $840 \text{ cm}^{-1}$  and C–N stretching at  $1219 \text{ cm}^{-1}$ ).<sup>[52,53]</sup> The high intensity of the C–N<sup>+</sup> stretching vibration at  $1337 \text{ cm}^{-1}$  suggested that PANi in the composites was in the doped state.<sup>[54]</sup> Raman footprints of PEDOT: PSS (i.e., stretching deformation of C $\beta$ –C $\beta$  at  $1372 \text{ cm}^{-1}$ , C $\alpha$ –C $\alpha$  interring stretching vibration at  $1256 \text{ cm}^{-1}$ , and oxyethylene ring deformations at  $577$  and  $994 \text{ cm}^{-1}$ )<sup>[55]</sup> were all present in the GO/PA-PE

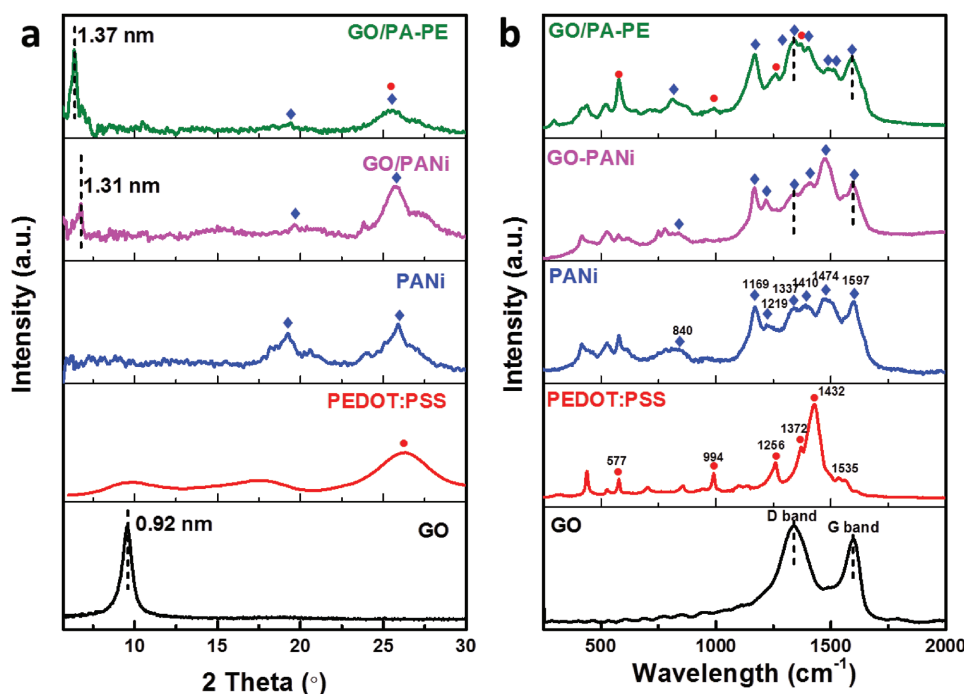


**Figure 3.** a) XRD pattern and b) Raman spectra of GO, PEDOT: PSS, PANi, GO/PANi, and GO/PA-PE samples.

composites. However, the D and G bands of the GO<sup>[11]</sup> were not obvious in the GO/PANi and GO/PA-PE composites. This could be because the GO sheets were totally covered by PANi and PEDOT: PSS which masked the D and G bands signals of the GO. FTIR spectroscopy also corroborated the Raman results (see Figure S8, Supporting Information, for detailed explanation of FTIR results).

## 2.2. Electrochemical Performance of Symmetric fMSCs

We fabricated symmetric fMSCs with interdigitated microelectrode patterns (Figure 4a) and evaluated their electrochemical performance. Briefly, GO/PA-PE composite inks with various GO/PANi loadings (from 20 to 50 wt%) were extrusion printed on top of prepatterned interdigitated Au tracks on PET film. Solid-state fMSCs were then assembled using a poly (vinyl alcohol) (PVA)-H<sub>3</sub>PO<sub>4</sub> electrolyte overcoat and electrical connections were established through copper tapes. fMSCs from pristine PEDOT: PSS and RGO-PE with 50 wt% GO loading were also prepared using this method for comparison (see Figure S9, Supporting Information, for RGO-PE ink viscosity and printed patterns). Tables S1 and S2 in the Supporting Information list the dimensions of the printed patterns and the mass loading of active materials for each fMSC device. The Au current collector was used to enhance the performance of our extrusion printed microelectrodes. A fMSC without the prepatterned Au tracks as current collector was also prepared via the same method and the performance was compared with the fMSC with Au current collector. It exhibited comparable capacitance with the fMSC with Au current collector when the scan rate is slow, e.g., 5 mV s<sup>-1</sup> (Figure S10, Supporting Information). We believe the Au current collector can be eliminated when other materials

with higher electrical conductivities are used as electrode materials. Evaluation of all devices revealed that the area of the cyclic voltammetry (CV) curves increased with GO/PA loading at all scan rates (5–500 mV s<sup>-1</sup>, Figure S11, Supporting Information). The GO/PANi loading of 50 wt% was therefore selected for the next experiments.

The optimal GO/PA-PE (with 50 wt% GO/PANi loading) fMSC showed superior performance over the neat PEDOT: PSS and RGO-PE fMSC in terms of capacitance, rate capability, energy, and power densities (Figure 4b–d). In GO/PA-PE fMSC, PEDOT: PSS serves as a conductive and flexible dispersant to facilitate ink preparation and the printing process and only contributes a small amount to fMSC capacitance (i.e., ≈3.32 F cm<sup>-3</sup> at 5 mV s<sup>-1</sup>). Most of the capacitance in the composite fMSCs comes from the active materials (i.e., rGO in RGO-PE and the well-ordered PANi on GO template in GO/PA-PE, respectively). The template function of GO in the GO/PA-PE composite materials was confirmed by comparing the performance with PANi-PEDOT/PSS materials (Figures S12 and S13, Supporting Information). The GO/PA-PE fMSC device exhibited two pronounced redox responses for PANi (i.e., the leucoemeraldine/emeraldine and emeraldine/pernigraniline structural transitions), enabling to achieve a higher capacitance than the RGO-PE fMSC device. Meanwhile, the larger capacitance and the quasi-square shape of the CV curves at all scan rates of 5–500 mV s<sup>-1</sup> (Figure 4c and Figure S14, Supporting Information) further demonstrate GO/PA-PE fMSC's fast charge transfer rate and excellent rate capability. The excellent performance of GO/PA-PE fMSC is also reflected in the Galvanostatic charge/discharge (GCD) curves (Figure S15, Supporting Information), electrochemical impedance spectra (EIS, Figure S16, Supporting Information), and energy and power densities (Figure 4d, calculated from the CV data based on the volume

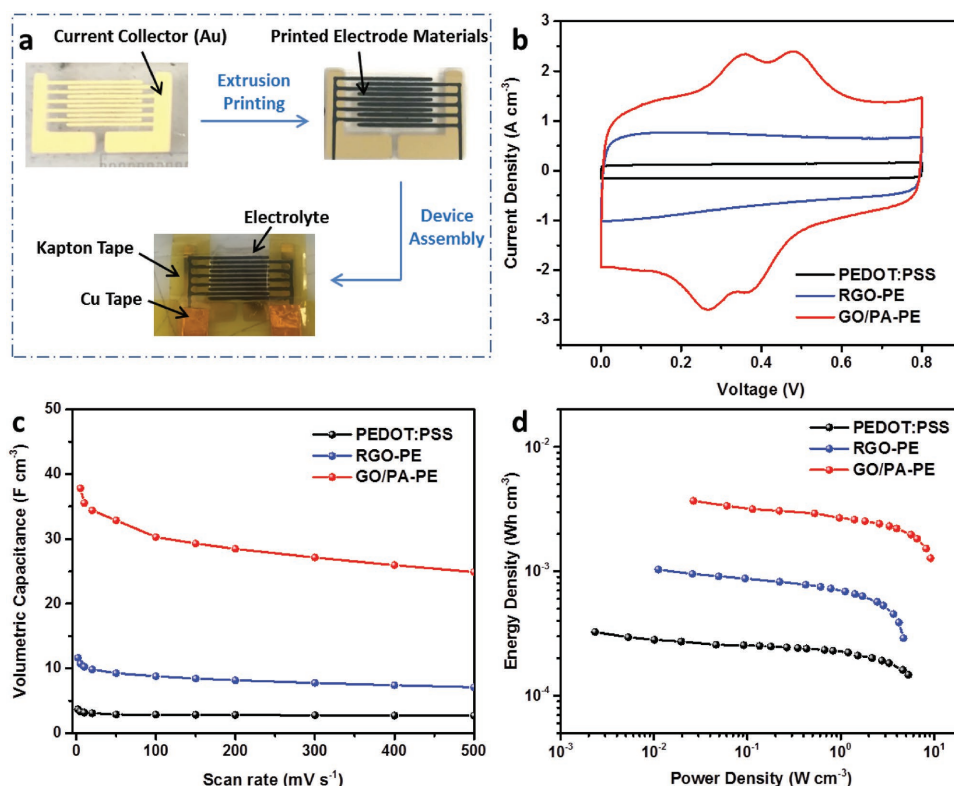


**Figure 4.** a) Schematic illustration of the fabrication of all-solid-state fMSCs on a flexible PET substrate using extrusion printing technique. b) CV curves at the scan rate of 50 mV s<sup>-1</sup>, c) device capacitance at different scan rates, and d) Ragone plots comparison the performance of GO/PA-PE, RGO-PE, and PEDOT: PSS fMSCs.

of the whole device). The GO/PA-PE fMSC also showed an energy density and a power density of  $\approx 3.36$  mWh cm<sup>-3</sup> and  $\approx 9.82$  W cm<sup>-3</sup>, respectively, which were found to be higher than the RGO-PE fMSC ( $\approx 1.03$  mWh cm<sup>-3</sup> and  $\approx 4.84$  W cm<sup>-3</sup>, respectively) and PEDOT: PSS fMSC ( $\approx 0.33$  mWh cm<sup>-3</sup> and  $\approx 5.3$  W cm<sup>-3</sup>, respectively).

The GO/PA-PE fMSC device exhibited an excellent volumetric capacitance of  $\approx 37.8$  F cm<sup>-3</sup> (areal capacitance  $\approx 17.5$  mF cm<sup>-2</sup>) at the scan rate of 5 mV s<sup>-1</sup> which was maintained  $\approx 80\%$  and  $\approx 66\%$  at the high scan rates of 100 and 500 mV s<sup>-1</sup>, respectively. When the scan rate increased from 5 to 500 mV s<sup>-1</sup>, the shape of the CV curve became slightly distorted and the redox peaks gradually weakened (Figure S14, Supporting Information). These observations can be attributed to the shorter ion diffusion time at high scan rates and increased electron transfer and ion diffusion path. The volumetric and areal performances of the GO/PA-PE fMSC device exceeds those of carbon-based fMSCs and are comparable with those of pseudocapacitive material-based fMSCs with sub-micrometer thickness, although less than 50 wt% PANi was used in the composite electrodes (see Table S3, Supporting Information for performance comparison of our fMSC with notable literature works). It is noteworthy that the areal capacitance is relatively low when compared with thicker pseudocapacitive fMSCs (with electrode thickness  $> 10$   $\mu$ m). That is because the GO/PA-PE fMSC was made from only two-layer extrusion printed microelectrodes with low electrode thickness of  $\approx 4.6$   $\mu$ m and active materials mass loading of  $\approx 0.28$  mg cm<sup>-2</sup>. The areal capacitance of the GO/PA-PE fMSC

is expected to be further increased with increasing the electrode thickness.

Extrusion printing is a simple technique to increase the interdigitated electrode thickness by repetitive layer-by-layer printing of electrode materials. The volume of extruded inks was kept the same per layer, so the mass loading of active materials increased linearly (from 0.28 to 2.8 mg cm<sup>-2</sup>) to the number of printing layers (from 2 to 20 layers). Accordingly, the electrode thickness increased from 4.6 to 80  $\mu$ m without expanding the finger electrode width (Figure S17, Supporting Information). The thickness of the electrode did not linearly increase with printing layers because the top layers of electrode finger became narrower and thicker than the bottom layers (Figure S18, Supporting Information). Upon exiting the printing nozzle, the printed ink lines not only spread laterally as they do on solid and smooth Au-PET substrate but they also spread downward into the porous bottom (previous) layer of the electrode materials. Therefore, the thicker the undried underneath layer, the less ink will spread along the lateral direction, resulting in narrowing the line width and increasing the line thickness. We evaluated the effect of printed layers on the areal device performance using CV measurements at different scan rates (from 5 to 500 mV s<sup>-1</sup>, Figure 5 and Figure S20, Supporting Information). We observed that at the low scan rate of 5 mV s<sup>-1</sup>, the area of the CV curve increased with the number of printed layers and all devices exhibited rectangular CV shape with the two pronounced redox peaks of PANi (Figure 5b). The analysis of CV results at this scan rate showed that the

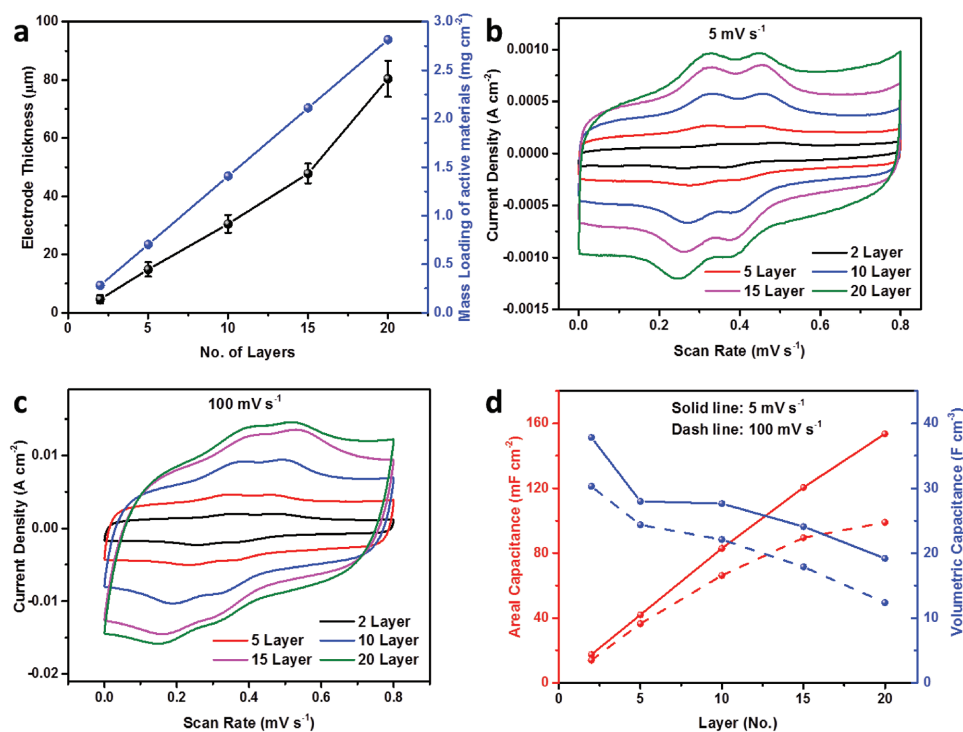


**Figure 5.** a) The relationship between the thickness and mass loading of electrode materials in fMSCs with printing layers. CV curves at the scan rates of b)  $5 \text{ mV s}^{-1}$  and c)  $100 \text{ mV s}^{-1}$ . d) Areal and volumetric capacitance of fMSCs with different printing layers.

areal capacitance of the fMSC device increased from  $17.5$  to  $153.6 \text{ mF cm}^{-2}$  with increasing the number of printed layers from 2 to 20 (Figure 5d, solid line). This increase in the areal capacitance indicates that the electrolyte ions had good access to the interior surface of the active materials. The 20-layer device maintained its superior areal performance at the high scan rate of  $100 \text{ mV s}^{-1}$  by showing a square shape CV and apparent redox peaks, indicating good rate capability performance (Figure 5c). The symmetric GCD curves suggest good capacitive characteristics of all devices at different current densities (Figure S22, Supporting Information). The increasing discharge times with printing layers indicate an increase in capacitance, which is consistent with the CV results.

The areal capacitance of  $153.6 \text{ mF cm}^{-2}$  at  $5 \text{ mV s}^{-1}$  and  $98.9 \text{ mF cm}^{-2}$  at  $100 \text{ mV s}^{-1}$  achieved on the 20-layer device are significantly higher than all fMSCs based on carbon and pseudocapacitive materials (Table S3, Supporting Information). The slightly decreased volumetric capacitances of  $19.2 \text{ F cm}^{-3}$  at  $5 \text{ mV s}^{-1}$  and  $12.4 \text{ F cm}^{-3}$  at  $100 \text{ mV s}^{-1}$  are also comparable with most of the carbon-based and pseudo-capacitive fMSCs (Table S3, Supporting Information). The constant increase in areal capacitance with thickness of the GO/PA-PE fMSCs is partly attributed to the porous hierarchical structure of the electrode materials. The other reason is the presence of the highly conductive and ion permeable PEDOT: PSS, which not only serves as a dispersing agent but also facilitates the penetration and transfer of electrolyte ions in between the inner surface of electrode materials. The decrease in volumetric capacitance with thickness was shown to be due to the increased electrode resistance and the reduced electrolyte penetration and ion transfer for thick and dense electrode.<sup>[18]</sup> It is notable that the

20-layer device also delivered an excellent areal energy density that was nearly ten times higher than the two-layer fMSC ( $15.4 \mu\text{Wh cm}^{-2}$  vs  $1.7 \mu\text{Wh cm}^{-2}$ , calculated from the CV data) without sacrificing the power density (increased from  $4.55$  to  $6.34 \text{ mW cm}^{-2}$ ), which is higher than most pseudo-capacitive fMSCs<sup>[16–18,28,56–58]</sup> (Figure S21 and Table S3, Supporting Information). The volumetric performance of the 20-layer fMSC with a decrease in volumetric energy density (from  $3.36$  to  $1.93 \text{ mW cm}^{-3}$ ) and power density (from  $9.82$  to  $0.79 \text{ W cm}^{-3}$ ) compared with the two-layer fMSC, were still comparable with the literature reports on thick (electrode thickness  $>10 \mu\text{m}$ ) fMSCs (Table S3, Supporting Information).

The interdigitated design also enhanced the overall device performance (both capacitance and rate capability), as the electrolyte ion could penetrate and diffuse along the parallel direction of the layered electrode materials in the interdigitated design as opposed to being limited to just the vertical direction in the conventional sandwiched design.<sup>[11,12,20]</sup> Therefore, the ion accessible surface of electrode and ion diffusion pathway will not be greatly affected in devices with thick electrodes, which can be confirmed by the nyquist plot of all fMSCs with different layers (see detailed explanation and Figure S23, Supporting Information). For comparison, we fabricated a supercapacitor device with the conventional sandwiched design by facing two GO/PA-PE films (with mass loading of  $1.4 \text{ mg cm}^{-2}$  per film) to each other and adding a layer of PVA/ $\text{H}_3\text{PO}_4$  gel electrolyte in between. The performance of the sandwiched-fMSC was compared with the 20-layer interdigitated-fMSC device that had the same total active materials mass loading of  $2.8 \text{ mg cm}^{-2}$  (see detailed parameter and device dimensions in Table S3, Supporting Information). The interdigitated-fMSC



showed a larger area in the CV curves at all scan rates investigated (from 2 to 500  $\text{mV s}^{-1}$ ) than the sandwiched-fMSC device (Figure S24, Supporting Information). The areal capacitance and volumetric of the interdigitated-fMSC device at 2  $\text{mV s}^{-1}$  was  $\approx 170 \text{ mF cm}^{-2}$  and  $21.7 \text{ F cm}^{-3}$  which was higher than that of the sandwiched-fMSC ( $\approx 100 \text{ mF cm}^{-2}$  and  $9.71 \text{ F cm}^{-3}$ ).

### 2.3. Asymmetric fMSCs

The device performance was further improved by making asymmetric fMSCs (AfMSCs). The fabrication of this device is practicable via extrusion printing. The positive (GO/PA-PE) and the negative (RGO-PE) electrodes were separately printed using two print-heads as illustrated in Figure 6a. Prior to printing, the charge balance between the two electrodes (i.e.,  $q_+ = q_-$ ) was carefully regulated to keep the stable operation of AfMSCs. Hence, the RGO-PE and GO/PA-PE electrodes were

first characterized to identify their stable potential range and specific capacitance (Figure S25, Supporting Information). On the basis of the Equations (S10) and (S11) in the Supporting Information, the optimal mass ratio between the two electrodes was measured as  $m_+/m_- = 0.52$ . It is obvious that the mass difference would inevitably cause volume differences of the two electrodes, which can be achieved by varying either the electrode thickness (named as AfMSC-T) or the electrode foot-print area (AfMSC-A). The AfMSC-T and AfMSC-A devices exhibited similar CV curves, indicating that the capacitance was the same for both devices (see Figure S27, Supporting Information, and the accompanying explanation). However, the AfMSC-A device exhibited superior volumetric performance due to the optimized space arrangement of the electrodes (Figures S26 and S27, Supporting Information) and was thus selected for further investigation.

Figure 6b shows the CV curves of the as-fabricated AfMSCs-A device with different operating voltage windows varying from

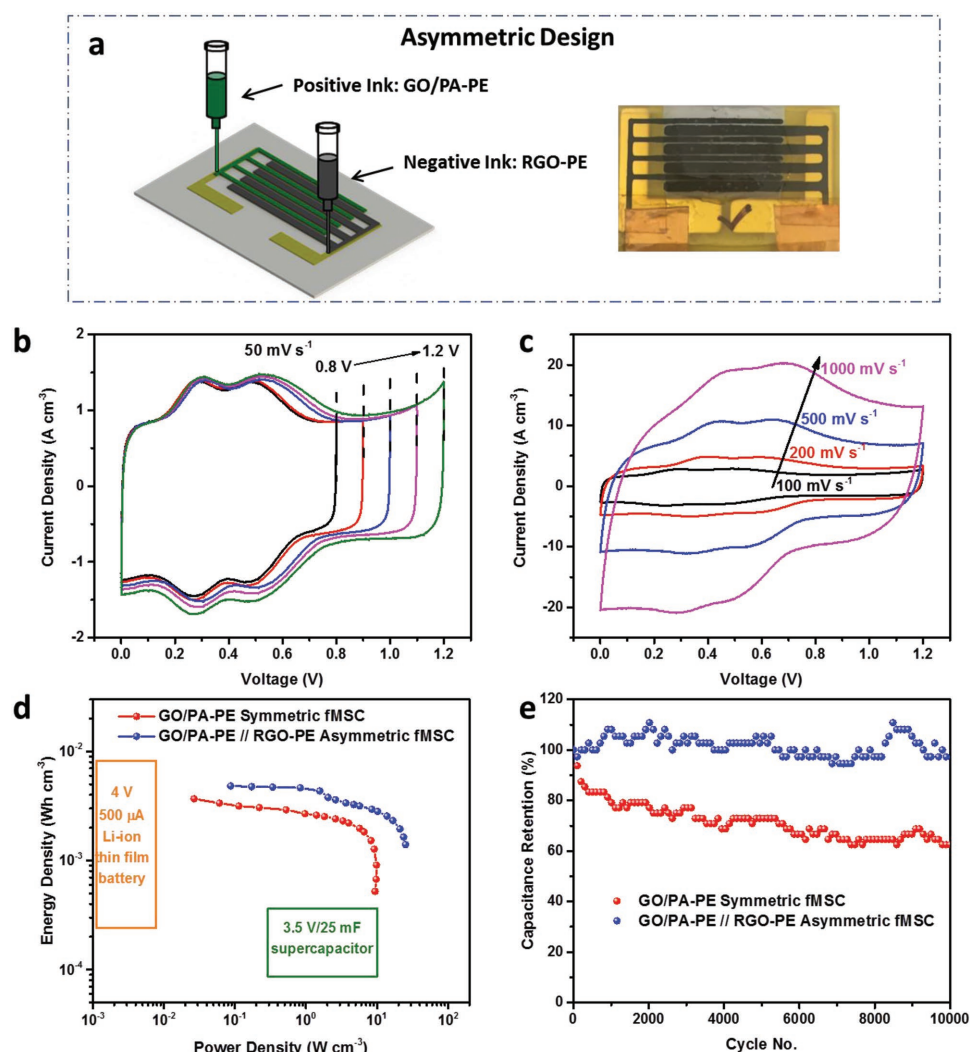


**Figure 6.** a) Schematic illustration and digital photograph of extrusion printed AfMSC. b) CV curves of AfMSCs measured at different voltage windows at a scan rate of 50  $\text{mV s}^{-1}$ . c) CV curves of AfMSCs at different scan rates (from 100 to 1000  $\text{mV s}^{-1}$ ) with a voltage window of 1.2 V. d) Ragone plots comparing GO/PA-PE symmetric fMSCs and AfMSCs. The data for Li-ion thin film battery and commercial supercapacitor were reproduced from reference.<sup>[23]</sup> e) Capacitance retention of the symmetric and asymmetric fMSCs during 10 000 cycles.



0–0.8 to 0–1.2 V at a scan rate of 50 mV s<sup>-1</sup>. The square shape and obvious redox peaks were observed in all CV curves, indicating that the voltage window can be increased from 0.8 to 1.2 V in asymmetric fMSCs. It is notable that these features of CV curves were retained even at a very high scan rate of 1000 mV s<sup>-1</sup> (Figure 6c). For the GO/PA-PE symmetric fMSCs these features could not be observed at the scan rates of higher than 500 mV s<sup>-1</sup> (Figure S14, Supporting Information). The enhancement in rate capability can be attributed to the better electrical conductivity of RGO-PE (82.8 S cm<sup>-1</sup>) than GO/PA-PE (64.01 S cm<sup>-1</sup>), which can also be seen from the smaller equivalent series resistance (ESR) of 14  $\Omega$  for asymmetric fMSCs compared with 21  $\Omega$  in the GO/PA-PE symmetric fMSCs (Figure S29, Supporting Information). The symmetric GCD curves and the calculated steady capacitance at all current densities (0.05–2 mA cm<sup>-2</sup>) also demonstrate the excellent AfMSC device performance, e.g., capacitive behavior and rate capability (Figure S28, Supporting Information).

The performance of AfMSCs was also compared with symmetric fMSCs using GO/PA-PE electrodes with similar mass loading of total active materials. The capacitance of the AfMSC (25 F cm<sup>-3</sup> at 5 mV s<sup>-1</sup>) was relatively lower than that of the GO/PA-PE symmetric fMSCs (37.8 F cm<sup>-3</sup> at 5 mV s<sup>-1</sup>). However, AfMSC showed higher energy density (from 3.36 to 4.83 mWh cm<sup>-3</sup>) and power density (from 9.4 to 25.3 W cm<sup>-3</sup>) compared to the symmetric fMSC, which illustrates the merits of the increased voltage window in AfMSC. This energy density is comparable to some commercial Li-ion thin film batteries but with a three orders of magnitude higher power density (Figure 6d). The AfMSC device also delivered significantly higher energy density and comparable power densities compared with commercial 3.5 V/25 mF supercapacitors. These values are also higher than some AfMSCs such as laser-induced graphene (LIG)-FeOOH/LIG-MnO<sub>2</sub>,<sup>[28]</sup> K<sub>2</sub>Co<sub>3</sub>(P<sub>2</sub>O<sub>7</sub>)<sub>2</sub>•2H<sub>2</sub>O/graphene,<sup>[34]</sup> most carbon-based symmetric fMSCs,<sup>[10,12,13,15,20–22]</sup> and some fMSCs based on pseudocapacitive materials<sup>[16,17,28,56,58]</sup> (Table S3, Supporting Information). Furthermore, the AfMSCs have better capacitance retention after long-term cycling than the symmetric fMSCs.

Similar to other literature reports,<sup>[28,59–61]</sup> some small fluctuations in capacitance were observed in the charge/discharge cycles when the applied current density became relatively high (690 mA cm<sup>-3</sup> for asymmetric and 550 mA cm<sup>-3</sup> for symmetric fMSCs). However, after 5000 consecutive cycles the capacitance retention of AfMSCs was almost 100% of its initial capacitance (charged up to 1.2 V), while the symmetric fMSCs only retained 70% of the initial capacitance (charged to 0.8 V). The values dropped to 96% and 65% respectively after 10 000 cycles. The instability of GO/PA-PE symmetric fMSC originates from the high current densities used in this study. At high current densities, PANi encounters fast redox reactions and rapid volume expansion during the charge/discharge process, which leaves PANi insufficient recovery time during each cycle. The excellent long cycle life of AfMSCs is due to the appropriate charge balance between the positive and negative electrodes, and the good electrochemical stability of the RGO-PE electrodes. The performance of the device was also tested under various bending conditions as performed in previous reports.<sup>[62–64]</sup> There is negligible change in the CV curves when the device was bent at various degrees (60° to 150°) or was subject to repeatedly bending at 150° for 1000 times (Figure S30, Supporting Information), indicating the excellent endurance to bending even during device operation.

## 2.4. Integration of Series and Parallel Designs

Multiple fMSCs can be connected together in series or parallel configurations to meet the current or voltage requirements that cannot be delivered by a single device. However, the electrical connections between fMSCs and the electrochemical isolation between single devices (i.e., electrolyte isolation) often involve additional fabrication steps (e.g., electrically connecting via conducting wires and making isolation mask using kapton tape). Our extrusion printing technique provides a facile solution for these issues. As shown in **Figure 7**, we can print both the interdigitated electrodes and the necessary connections between the devices using extrusion printing. We also extrusion-printed

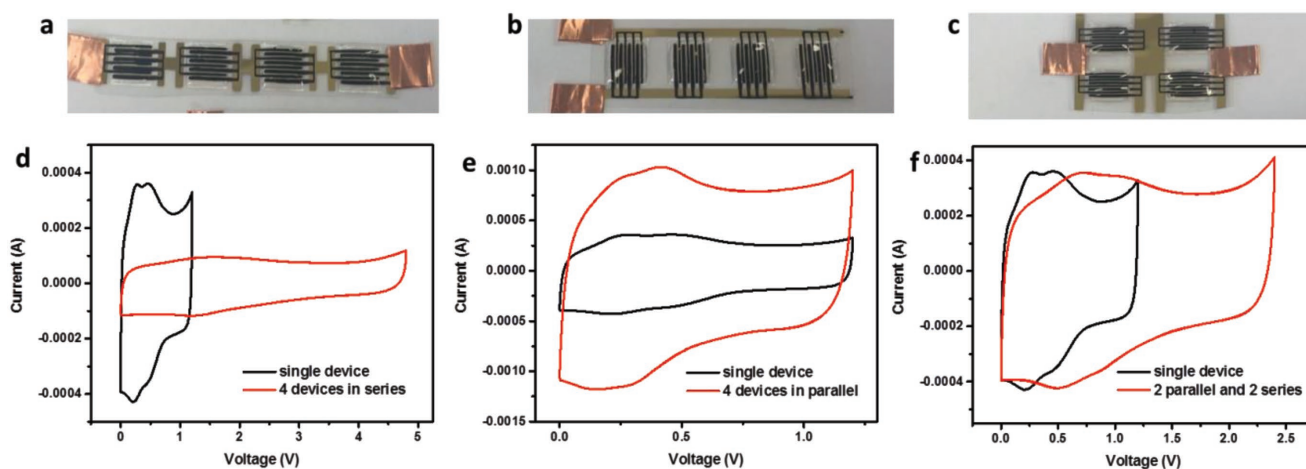


**Figure 7.** a–c) Photos of four connected fMSCs on PET film. a) In series, b) in parallel, and c) in a combination of series and parallel. d–f) CV curves of the fMSC devices shown in (a–c) at the scan rate of 100 mV s<sup>-1</sup>.

the PDMS cell barriers which acted as repellent to the wet polymer gel electrolyte and enabled electrochemical isolation of fMSCs that were positioned close to each other. Figure 7 shows the performance of devices made by using four AfMSCs in series, parallel, and a combination of these two configurations. A wide voltage window of 4.8 V was achieved connecting the four AfMSCs in series (Figure 7a). When the four AfMSCs were connected in parallel configuration, the output current increased four times compared with the single fMSC in CV curves (Figure 7b). The combination of two series and two parallel connections increased the voltage window to 2.4 V without decreasing the output current in CV curves (Figure 7c). The GCD curves (Figure S31, Supporting Information) also show that it is possible to enhance the output voltage and discharge time by connecting several devices in series and parallel respectively (Figure S31, Supporting Information). These results suggest the excellent connection between individual devices.

### 3. Conclusion

We have developed extrusion printable GO/PANi and rGO inks with the assistance of the PEDOT: PSS stabilizer. The use of PEDOT: PSS not only improved the printability of the active materials (i.e., GO/PANi and rGO) in terms of water stability and viscosity but also endowed the composition with high electrical conductivity and enabled the full utilization of inner surface capacitance. The extrusion printed GO/PA-PE-based symmetric fMSCs exhibited high areal capacitance ( $153.6 \text{ mF cm}^{-2}$  at  $5 \text{ mV s}^{-1}$ ) and volumetric capacitance ( $19.2 \text{ F cm}^{-3}$  at  $5 \text{ mV s}^{-1}$ ) which were higher or comparable to the literature values. The extrusion printed AfMSCs with GO/PANi-PEDOT: PSS and graphene-PEDOT: PSS as positive and negative materials, respectively showed a voltage window of 1.2 V and an energy density and power density of  $4.83 \text{ mWh cm}^{-3}$  and  $25.3 \text{ W cm}^{-3}$  which were significantly higher than those of symmetric fMSCs. In addition, the AfMSC showed 100% capacitance retention over 5000 cycles due to the appropriate charge balance between the two electrodes. This work demonstrated that it is possible use extrusion printing to fabricate asymmetric fMSCs. Further improvements of negative electrode materials can widen the voltage window (beyond 1.2 V) and lead to higher device capacitance. Extrusion printing also enables the fabrication of several connected fMSCs on a substrate, which made it practical for real applications that require higher currents or voltages. The ink preparation process and the device fabrication technique presented in this work are facile and highly scalable. Therefore, the high-performance extrusion printed fMSCs are especially promising for use as power sourced that can be directly integrated into the next-generation of printed wearable microelectronics. Inks of current collectors (inkjet printable silver nanowires<sup>[65]</sup> and screen printable silver paint<sup>[66]</sup>) and electrolyte (inkjet printable poly(4-styrenesulfonic acid) (PSSH)<sup>[33]</sup> and ionic liquid polymer gel electrolyte<sup>[65]</sup>) have also been developed and can be used to prepare fully printed fMSCs. This will increase the simplicity and scalability of the fabrication of fMSCs. We believe that the fully extrusion printed fMSCs is a promising area of research area in the near future.

### 4. Experimental Section

**Materials:** Graphite flakes, PVA ( $M_w$ : 146 000–186 000), aniline monomer, ammonia persulfate (APS), and potassium permanganate were purchased from Sigma-Aldrich. Concentrated sulfuric acid ( $\text{H}_2\text{SO}_4$ , 98%), orthophosphoric acid ( $\text{H}_3\text{PO}_4$ , 85%), hydrochloric acid (HCl, 32%), hydrogen peroxide ( $\text{H}_2\text{O}_2$ , 30%), chloroform, and ethanol (100%) were obtained from Chem-Supply. PEDOT: PSS redispersible pellets (Orgacon DRY) were purchased from Agfa.

**GO/PANi Composite:** GO/PANi composite was synthesized by an interfacial polymerization method.<sup>[67–69]</sup> Typically, GO ( $\approx 120 \text{ mg}$ , prepared by improved Hummers method<sup>[61–70]</sup>) was dispersed into  $\approx 200 \text{ mL}$  of  $1 \text{ M H}_2\text{SO}_4$  and the mixture was bath sonicated (Branson B5500R-DTH, 175 W) for 30 min to obtain a well-dispersed suspension. Then APS ( $\approx 5.70 \text{ g}$ ) was dissolved in the above solution by further sonicating for 30 min to form the water phase. Aniline monomers ( $\approx 2.30 \text{ g}$ ) were dissolved in  $\approx 200 \text{ mL}$  of chloroform by bath sonicating for 5 min to form an organic phase. The organic and water phases were then carefully transferred to a 2 L beaker successively and the reaction was performed at room temperature for  $\approx 5 \text{ h}$ , during which the initial yellow-brown water-phase gradually changed to dark green. The resulting product in the water phase was centrifuged (Eppendorf centrifuge 5702) at 4400 rpm for 10 min and then washed three times with ethanol and deionized water by further centrifugation (at 4400 rpm for 20 min).

**GO/PA-PE Ink Formulation:** The as-prepared GO/PANi composite, obtained from the above centrifugation, was dispersed in  $\approx 100 \text{ mL}$  deionized water and bath sonicated for 3 h. The concentration of the GO/PANi dispersion was then increased by rotary evaporation. The GO/PA-PE dispersion with various GO/PANi mass loadings from 20 to 80 wt% were achieved by adding desired amounts of PEDOT: PSS pellets to the above GO/PANi dispersion, overnight stirring, and bath sonication for 20 min. The solid content of PEDOT: PSS was maintained at  $25 \text{ mg mL}^{-1}$  to form slurry-like ink in all GO/PA-PE ink formulation.

**rGO-PE Ink Formulation:** The rGO-PEDOT: PSS dispersion was prepared according to the method that was reported previously.<sup>[25]</sup> The concentration of the dispersion was increased to  $\approx 21 \text{ mg mL}^{-1}$  by rotary evaporation for the use as an ink for extrusion printing.

**Extrusion Printing of fMSCs:** Symmetric fMSCs were produced by directly extrusion printing of active materials on Au prepatterned PET film as illustrated in Figure 3a. A thin layer of Au (200 nm) was sputter coated on a flexible PET film through the custom-made interdigital finger mask with two square-shaped contact pads to connect to the positive and negative electrodes. The as-prepared inks were then carefully printed on the prepatterned Au using an extrusion printer (KIMM SPS1000, Figure S30, Supporting Information) with X-Y-Z motion control system and positioning resolution of  $1 \mu\text{m}$ . A dispensing tip ( $100 \mu\text{m}$  in inner nozzle diameter) was used to print the inks at an applied gas pressure ranging from 5 to 30 kPa (pressure varied for different dispersion to keep the flow rate at  $\approx 5 \mu\text{L min}^{-1}$ ). The tip moving speed was set at  $400 \text{ mm min}^{-1}$  and the tip-to-substrate distance was varied from 50 to  $100 \mu\text{m}$ . To facilitate the solvent evaporation, the substrate was heated to  $40^\circ\text{C}$  during the printing process. After printing, the printed electrodes were dried in an oven at  $60^\circ\text{C}$  overnight (in air) to remove all solvents. In order to assemble the extrusion printed patterned electrodes into all-solid-state fMSCs, the two Au contact pads were first extended with conductive copper tapes to prevent the Au contact pads from being scratched by electric wire clamps and to provide electrical connection to the electrochemical workstation for testing. A hot PVA- $\text{H}_3\text{PO}_4$  polymer gel electrolyte (heated to  $85^\circ\text{C}$  prior to use) was then cast onto the interdigitated electrodes while the rest of the electrodes and copper tapes had been covered by Kapton polyimide tape to prevent contact with the electrolyte. The all-solid-state fMSCs were ready to test after air-drying the electrolyte overnight. The PVA- $\text{H}_3\text{PO}_4$  electrolyte was prepared according to the previously reported method.<sup>[25]</sup> PVA powder (4 g),  $\text{H}_3\text{PO}_4$  (6 g), and deionized water (40 mL) were mixed together and then heated to around  $85^\circ\text{C}$  under magnetic stirring until the solution became clear.

The asymmetric fMSCs with GO/PANi-PEDOT: PSS as the positive electrode and rGO-PEDOT: PSS as the negative electrode were assembled similarly. The only difference was that in the extrusion printing process, the positive and negative inks were stored in separate syringes and printed separately on the prepatterned Au current collectors.

**Characterization:** The extrusion printed patterns, microelectrodes, and ink dispersions were observed under optical microscopy (Leica DM600). The surface and cross-section morphology of the composites and printed films were investigated using a field emission scanning electron microscope (SEM, JEOL JSM-7500FA). A surface profilometer (Veeco Dektak 150) was used to measure the thicknesses of the printed patterns, which were then used to measure the sheet resistance using a four-probe conductivity meter (Jandel RM3-AR). XRD patterns were acquired using a GBC MMA XRD with a Cu  $K_{\alpha}$  radiation ( $\lambda = 1.54 \text{ \AA}$ ) at the voltage and current of 40 kV and 25 mA, respectively. Raman spectroscopy was performed on a Jobin-Yvon Horiba 800 equipped with He-Ne laser (632.81 nm excitation). UV-vis spectroscopy was performed with a UV spectrophotometer (UV-1800, Shimadzu). The rheological properties of the inks were measured using a rheometer (AR-G2, TA Instruments) with a cone and plate geometry (15 mm cone diameter,  $2^{\circ}1'57''$  cone angle, and 55  $\mu\text{m}$  truncation).

The electrochemical performances of the fMSCs were investigated using CV, EIS, and GCD techniques. CVs were performed using a CHI720 electrochemical workstation. GCD and long-term cycling tests were carried out with a Neware Galvanosta (10 mA, 5 V). EIS data were obtained using an impedance analyzer (Solartron SI1260) and a potentiostat/galvanostat (EG&G Model 283, Princeton Applied Research) at the open circuit potential and the AC amplitude of 10 mV on the frequency range of 0.01 Hz to 1 MHz.

## Supporting Information

Supporting Information is available from the Wiley Online Library or from the author.

## Acknowledgements

Funding from the Australian Research Council (ARC) Centre of Excellence Scheme (CE 140100012) is gratefully acknowledged. The authors would like to thank the Australian National Fabrication Facility—Materials node for materials and printing process and University of Wollongong (UOW) Electron Microscopy Centre for equipment use. G.G.W. and J.M.R. gratefully acknowledge the ARC for support under the Australian Laureate Fellowship (FL110100196) and Future Fellowship (FT130100380) schemes, respectively. Y.L. would like to acknowledge the scholarship support from China Scholarship Council (CSC).

## Conflict of Interest

The authors declare no conflict of interest.

## Keywords

extrusion printing, graphene, microsupercapacitors, polyaniline, printable ink

Received: November 12, 2017

Revised: January 29, 2018

Published online:

- [1] J. M. Miller, *Ultracapacitor Applications*, The Institution of Engineering and Technology, London, UK **2011**.
- [2] D. Pech, M. Brunet, H. Durou, P. Huang, V. Mochalin, Y. Gogotsi, P.-L. Taberna, P. Simon, *Nat. Nanotechnol.* **2010**, *5*, 651.
- [3] X. Lang, A. Hirata, T. Fujita, M. Chen, *Nat. Nanotechnol.* **2011**, *6*, 232.
- [4] Y. Masaki, J. B. Ralph, K. Akiya, *Lithium-Ion Batteries, Science and Technologies*, Springer, New York, USA **2009**.
- [5] Z. L. Wang, *Nano Today* **2010**, *5*, 512.
- [6] I. F. Akyildiz, W. Su, Y. Sankarasubramaniam, E. Cayirci, *Comput. Networks* **2002**, *38*, 393.
- [7] J.-H. Sung, S.-J. Kim, S.-H. Jeong, E.-H. Kim, K.-H. Lee, *J. Power Sources* **2006**, *162*, 1467.
- [8] J. Chmiola, C. Largeot, P.-L. Taberna, P. Simon, Y. Gogotsi, *Science* **2010**, *328*, 480.
- [9] P. Huang, M. Heon, D. Pech, M. Brunet, P.-L. Taberna, Y. Gogotsi, S. Lofland, J. D. Hettinger, P. Simon, *J. Power Sources* **2013**, *225*, 240.
- [10] Z.-S. Wu, K. Parvez, A. Winter, H. Vieker, X. Liu, S. Han, A. Turchanin, X. Feng, K. Müllen, *Adv. Mater.* **2014**, *26*, 4552.
- [11] Z. Niu, L. Zhang, L. Liu, B. Zhu, H. Dong, X. Chen, *Adv. Mater.* **2013**, *25*, 4035.
- [12] Z.-S. Wu, K. Parvez, X. Feng, K. Müllen, *Nat. Commun.* **2013**, *4*, 2487.
- [13] W.-W. Liu, Y.-Q. Feng, X.-B. Yan, J.-T. Chen, Q.-J. Xue, *Adv. Funct. Mater.* **2013**, *23*, 4111.
- [14] J. Lin, C. Zhang, Z. Yan, Y. Zhu, Z. Peng, R. H. Hauge, D. Natelson, J. M. Tour, *Nano Lett.* **2013**, *13*, 72.
- [15] M. Beidaghi, C. Wang, *Adv. Funct. Mater.* **2012**, *22*, 4501.
- [16] K. Wang, W. J. Zou, B. G. Quan, A. F. Yu, H. P. Wu, P. Jiang, Z. X. Wei, *Adv. Energy Mater.* **2011**, *1*, 1068.
- [17] X. Wang, B. D. Myers, J. Yan, G. Shekawat, V. Dravid, P. S. Lee, *Nanoscale* **2013**, *5*, 4119.
- [18] Z. Wu, K. Parvez, S. Li, S. Yang, Z. Liu, S. Liu, X. Feng, K. Müllen, *Adv. Mater.* **2015**, *27*, 1521.
- [19] W. Liu, C. Lu, X. Wang, R. Y. Tay, K. Tay, *ACS Nano* **2015**, *9*, 1528.
- [20] M. F. El-Kady, R. B. Kaner, *Nat. Commun.* **2013**, *4*, 1475.
- [21] Z. Peng, R. Ye, J. A. Mann, D. Zakhidov, Y. Li, P. R. Smalley, J. Lin, J. M. Tour, *ACS Nano* **2015**, *9*, 5868.
- [22] J. Lin, Z. Peng, Y. Liu, F. Ruiz-Zepeda, R. Ye, E. L. G. Samuel, M. J. Yacamán, B. I. Yakobson, J. M. Tour, *Nat. Commun.* **2014**, *5*, 5714.
- [23] H.-C. Huang, C.-J. Chung, C.-T. Hsieh, P.-L. Kuo, H. Teng, *Nano Energy* **2016**, *21*, 90.
- [24] P. Yadav, A. Basu, A. Suryawanshi, O. Game, S. Ogale, *Adv. Mater. Interfaces* **2016**, *3*, 1600057.
- [25] Y. Liu, B. Weng, Q. Xu, Y. Hou, C. Zhao, S. Beirne, K. Shu, R. Jalili, G. G. Wallace, J. M. Razal, J. Chen, *Adv. Mater. Technol.* **2016**, *1*, 1600166.
- [26] Y.-Y. Peng, B. Akuzum, N. Kurra, M.-Q. Zhao, M. Alhabeb, B. Anasori, E. C. Kumbur, H. N. Alshareef, M.-D. Ger, Y. Gogotsi, M. Beidaghi, Y. Gogotsi, *Energy Environ. Sci.* **2016**, *9*, 2847.
- [27] N. Kurra, B. Ahmed, Y. Gogotsi, H. N. Alshareef, *Adv. Energy Mater.* **2016**, *6*, 1601372.
- [28] L. Li, J. Zhang, Z. Peng, Y. Li, C. Gao, Y. Ji, R. Ye, N. D. Kim, Q. Zhong, Y. Yang, H. Fei, G. Ruan, J. M. Tour, *Adv. Mater.* **2016**, *28*, 838.
- [29] M. F. El-Kady, M. Ihns, M. Li, J. Y. Hwang, M. F. Mousavi, L. Chaney, A. T. Lech, R. B. Kaner, *Proc. Natl. Acad. Sci. U. S. A.* **2015**, *112*, 4233.
- [30] X. Tian, J. Jin, S. Yuan, C. K. Chua, S. B. Tor, K. Zhou, *Adv. Energy Mater.* **2017**, *7*, 1700127.
- [31] K. Fu, Y. Yao, J. Dai, L. Hu, *Adv. Mater.* **2017**, *29*, 1603486.
- [32] W. Yu, H. Zhou, B. Q. Li, S. Ding, *ACS Appl. Mater. Interfaces* **2017**, *9*, 4597.

- [33] J. Li, S. Sollami Delekta, P. Zhang, S. Yang, M. R. Lohe, X. Zhuang, X. Feng, M. Östling, *ACS Nano* **2017**, *11*, 8249.
- [34] H. Pang, Y. Zhang, W.-Y. Lai, Z. Hu, W. Huang, *Nano Energy* **2015**, *15*, 303.
- [35] G. Sun, J. An, C. K. Chua, H. Pang, J. Zhang, P. Chen, *Electrochem. Commun.* **2015**, *51*, 33.
- [36] E. B. Secor, P. L. Prabhumirashi, K. Puntambekar, M. L. Geier, M. C. Hersam, *J. Phys. Chem. Lett.* **2013**, *4*, 1347.
- [37] J. Li, F. Ye, S. Vaziri, M. Muhammed, M. C. Lemme, M. Östling, *Adv. Mater.* **2013**, *25*, 3985.
- [38] E. B. Secor, T. Z. Gao, A. E. Islam, R. Rao, S. G. Wallace, J. Zhu, K. W. Putz, B. Maruyama, M. C. Hersam, *Chem. Mater.* **2017**, *29*, 2332.
- [39] N. Behabtu, J. R. Lomeda, M. J. Green, A. L. Higginbotham, A. Sinitskii, D. V. Kosynkin, D. Tsentelovich, A. N. G. Parra-Vasquez, J. Schmidt, E. Kesselman, Y. Cohen, Y. Talmon, J. M. Tour, M. Pasquali, *Nat. Nanotechnol.* **2010**, *5*, 406.
- [40] J. Jang, J. Ha, J. Cho, *Adv. Mater.* **2007**, *19*, 1772.
- [41] J. Huang, R. B. Kaner, *J. Am. Chem. Soc.* **2004**, *126*, 851.
- [42] O. Ngamna, A. Morrin, A. J. Killard, S. E. Moulton, M. R. Smyth, G. G. Wallace, *Langmuir* **2007**, *23*, 8569.
- [43] D. Li, R. B. Kaner, *Chem. Commun.* **2005**, 3286.
- [44] P. Shi, R. Chen, L. Hua, L. Li, R. Chen, Y. Gong, C. Yu, J. Zhou, B. Liu, G. Sun, W. Huang, *Adv. Mater.* **2017**, *29*, 1703455.
- [45] S. J. Yoo, J. Cho, J. W. Lim, S. H. Park, J. Jang, Y.-E. Sung, *Electrochem. Commun.* **2010**, *12*, 164.
- [46] G. C. Pidcock, M. in het Panhuis, *Adv. Funct. Mater.* **2012**, *22*, 4790.
- [47] K. Fu, Y. Wang, C. Yan, Y. Yao, Y. Chen, J. Dai, S. Lacey, Y. Wang, J. Wan, T. Li, Z. Wang, Y. Xu, L. Hu, *Adv. Mater.* **2016**, *28*, 2587.
- [48] R. Darby, *Chemical Engineering Fluid Mechanics*, 3rd ed., CRC Press, Boca Raton, FL **2017**.
- [49] W. J. Hyun, E. B. Secor, C.-H. Kim, M. C. Hersam, L. F. Francis, C. D. Frisbie, *Adv. Energy Mater.* **2017**, *7*, 1700285.
- [50] L. Yuan, B. Yao, B. Hu, K. Huo, W. Chen, J. Zhou, *Energy Environ. Sci.* **2013**, *6*, 470.
- [51] K. Zhang, L. L. Zhang, X. S. Zhao, J. Wu, *Chem. Mater.* **2010**, *22*, 1392.
- [52] T. Lindfors, C. Kvarnström, A. Ivaska, *J. Electroanal. Chem.* **2002**, *518*, 131.
- [53] M. Bláha, M. Riesová, J. Zedník, A. Anžlovar, M. Žigon, J. Vohlídal, *Synth. Met.* **2011**, *161*, 1217.
- [54] D. Li, Y. Li, Y. Feng, W. Hu, W. Feng, *J. Mater. Chem. A* **2015**, *3*, 2135.
- [55] X. Zhang, D. Chang, J. Liu, Y. Luo, *J. Mater. Chem.* **2010**, *20*, 5080.
- [56] B. Song, L. Li, Z. Lin, Z.-K. Wu, K. Moon, C.-P. Wong, *Nano Energy* **2015**, *16*, 470.
- [57] M. Zhu, Y. Huang, Y. Huang, H. Li, Z. Wang, Z. Pei, Q. Xue, H. Geng, C. Zhi, *Adv. Mater.* **2017**, *29*, 1605137.
- [58] J. Yun, Y. Lim, G. N. Jang, D. Kim, J. Lee, H. Park, S. Yeong, G. Lee, G. Zi, J. Sook, *Nano Energy* **2015**, *19*, 401.
- [59] D. Antiohos, M. S. Romano, J. M. Razal, S. Beirne, P. Aitchison, A. I. Minett, G. G. Wallace, J. Chen, *J. Mater. Chem. A* **2014**, *2*, 14835.
- [60] D. Antiohos, G. Folkes, P. Sherrell, S. Ashraf, G. G. Wallace, P. Aitchison, A. T. Harris, J. Chen, A. I. Minett, *J. Mater. Chem.* **2011**, *21*, 15987.
- [61] Y. Liu, B. Weng, J. M. Razal, Q. Xu, C. Zhao, Y. Hou, S. Seyedin, R. Jalili, G. G. Wallace, J. Chen, *Sci. Rep.* **2015**, *5*, 17045.
- [62] H. Li, Y. Hou, F. Wang, M. R. Lohe, X. Zhuang, L. Niu, X. Feng, *Adv. Energy Mater.* **2017**, *7*, 1601847.
- [63] P. Zhang, F. Zhu, F. Wang, J. Wang, R. Dong, X. Zhuang, O. G. Schmidt, X. Feng, *Adv. Mater.* **2017**, *29*, 1604491.
- [64] C. Yang, K. S. Schellhammer, F. Ortmann, S. Sun, R. Dong, M. Karakus, Z. Mics, M. Löffler, F. Zhang, X. Zhuang, E. Cánovas, G. Cuniberti, M. Bonn, X. Feng, *Angew. Chem., Int. Ed.* **2017**, *56*, 3920.
- [65] K.-H. Choi, J. Yoo, C. K. Lee, S.-Y. Lee, *Energy Environ. Sci.* **2016**, *9*, 2812.
- [66] Y. Wang, Y. Shi, C. X. Zhao, J. I. Wong, X. W. Sun, H. Y. Yang, *Nanotechnology* **2014**, *25*, 94010.
- [67] J. C. Michaelson, A. J. McEvoy, *J. Chem. Soc. Chem. Commun.* **1994**, 323, 79.
- [68] J. Zhu, M. Chen, H. Qu, X. Zhang, H. Wei, Z. Luo, H. A. Colorado, S. Wei, Z. Guo, *Polymer* **2012**, *53*, 5953.
- [69] J. Shen, C. Yang, X. Li, G. Wang, *ACS Appl. Mater. Interfaces* **2013**, *5*, 8467.
- [70] D. C. Marcano, D. V. Kosynkin, J. M. Berlin, A. Sinitskii, Z. Sun, A. Slesarev, L. B. Alemany, W. Lu, J. M. Tour, *ACS Nano* **2010**, *4*, 4806.